A Dynamic Model for Concentric Tube Robots

John Till¹, Student Member, IEEE, Vincent Aloi¹, Student Member, IEEE, Katherine E. Riojas², Student Member, IEEE, Patrick L. Anderson², Student Member, IEEE, Robert J. Webster III², Senior Member, IEEE, and Caleb Rucker¹, Member, IEEE

Abstract—Existing static and kinematic models of concentric tube robots are based on the ordinary differential equations of a static Cosserat rod. In this paper, we provide the first dynamic model for concentric tube continuum robots by adapting the partial differential equations of a dynamic Cosserat rod to describe the coupled inertial dynamics of precurved concentric tubes. This generates an initial-boundary-value problem that can capture robot vibrations over time. We solve this model numerically at high time resolutions using implicit finite differences in time and arc length. This approach is capable of resolving the high-frequency torsional dynamics that occur during unstable "snapping" motions and provides a simulation tool that can track the true robot configuration through such transitions. Further, it can track slower oscillations associated with bending and torsion as a robot interacts with tissue at real-time speeds. Experimental verification of the model shows that this wide range of effects is captured efficiently and accurately.

I. INTRODUCTION

Concentric tube robots (CTRs) are needle-sized continuum robots consisting of nested, precurved elastic tubular structures [1]. When these concentric structures are rotated and translated relative to one another, their curvatures interact elastically to control the shape and pose of the robot. These robots are scalable and customizable, since elastic tubes comprise the entire robot, and such tubes are available at a variety of diameters and can even be 3D printed in custom shapes [2]. These features have led to promising proof of concept demonstrations in a variety of minimally invasive surgical applications [3], [4], [1] where CTRs are primarily used either as steerable needles (see e.g. [5], [6], [7]) or miniature manipulators (see e.g. [8], [9], [10], [11]).

To enable effective use of CTRs, models of these robots have rapidly advanced in the last decade. While some alternate approaches have been proposed, such as finite shell element modeling [12], a large majority of this work has been based on the equations of a *static* Cosserat rod, describing the

This material is based upon work supported by the National Science Foundation under CAREER Award IIS-1652588 and Graduate Research Fellowship DGE-1445197, and by the National Institutes of Health in part by the National Institute of Biomedical Imaging and Bioengineering training grant T32-EB021937 and research grant R01-EB026901. Any opinion, findings, and conclusions or recommendations expressed in this material are those of the authors and do not necessarily reflect the views of the National Science Foundation or National Institutes of Health.

¹J. Till, V. Aloi, and C. Rucker are with the Department of Mechanical, Aerospace, and Biomedical Engineering, The University of Tennessee, Knoxville, TN (e-mail: JTill@vols.utk.edu, Caleb.Rucker@utk.edu)

²K. Riojas, P. Anderson, and R. J. Webster III are with the Department of Mechanical Engineering, Vanderbilt University, Nashville, TN 37235 USA (e-mail: katherine.e.riojas@vanderbilt.edu, Robert.Webster@vanderbilt.edu)

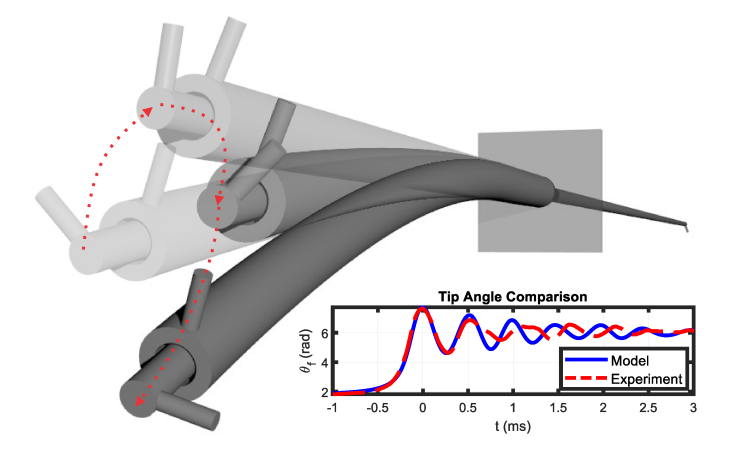


Fig. 1. A rendering of our model solution showing the concentric tube robot undergoing an elastic instability. The dynamic model in this paper describes the robots oscillations during this motion for the first time.

internal bending and torsion of component tubes [13], [14], [15] (for a review see [1]). In general, a system of differential equations in arc length is created by writing the rod equation for each component tube and enforcing a shared centerline constraint such that the tubes conform to the same curvature as a function of arc length. The result of this constraint is a set of differential equations and boundary conditions, the solution to which yields the axial tube angles and the position and orientation along the robot as a function of arc length, for a given set of tube base angular and linear positions (i.e., the variables commanded by actuators). External loading can naturally be incorporated into this model through the Cosserat rod equations [15], [16]. When normalized with respect to arc length, resulting accuracy has been shown to be as high as 1% to 3% of total arc length [15], [13]. The static model framework can be used to formulate and solve forward kinematics [15], [13], inverse kinematics [17], [18], control [10], [19], and sensing [20], [4] problems. Shooting methods and efficient linearization can increase computational speed [21], [10]. While the field has been able to make substantial progress with quasistatic models, dynamic models have yet to be developed, and will enable CTRs to advance in a number of important ways.

First, a dynamic model can help describe interactions between the robot and objects in its environment that can be dynamically modeled, such as tissue in surgery. Transitions between contact states (e.g. if a robot is holding an object and suddenly releases it, or pulling on a piece of tissue to cut resulting in elastic energy release) may induce significant robot vibration. We experimentally validate our model in this type of scenario in Section V. A dynamic model provides a basis for a dynamic controller that could mitigate the bending vibrations that occur when the robot is manipulating tissue.

Second, since a dynamic model deals with the time history of the entire robot state, it provides a framework in which it is feasible to incorporate possible hysteresis phenomena such as friction. Concentric-tube friction is only just beginning to be studied and has so far been handled using lumped parameter approaches [22], or assuming uni-directional actuation histories [23]. In this paper, we investigate a simple Coulomb plus viscous friction model, using assumptions similar to [22] but in a new dynamic context.

Third, concentric tube robots exhibit elastic instabilities in which the robot snaps from one configuration to another, rapidly releasing stored strain energy [24], [25], as illustrated in Figure 1. While usually something to be avoided, it has been shown that snapping can be harnessed beneficially under certain conditions [26]. This event entails a highly dynamic transition between two different static states. While unstable regimes can be predicted [24], [25] and avoided by design ([27], [28], [29], [30], [18]), path planning ([31], [32]), and control ([17], [33]), the transition behavior itself has never been modeled, and quasi-static models fail to appropriately resolve the instability as shown in Figure 2. Modeling the robot state during the dynamic snap transition can provide insights about the severity of the snap (e.g. velocities, displacement overshoot). This simulation capability is potentially useful to analyze the design space of CTRs and expand it to include robots that have relatively benign snapping behavior (i.e some snapping instabilities may be very gentle and acceptable in practice). Further, one could intentionally design a robot such that its open-loop snapping behavior naturally delivers a desired velocity in a given puncture task. A dynamic simulation tool is necessary to give knowledge to the designer in both cases.

A. Contributions and Prior Work

In prior work, we have used the partial differential equations of a dynamic Cosserat rod to derive tendon-actuated robot models [34], and we have recently proposed a new implicit method for solving the dynamic single-rod equations efficiently in real-time [35] and applied this method to pneumatic, parallel-rod, and tendon-actuated robots in [36]. However, concentric-tube robots have a fundamentally different structure with multiple precurved tubes constrained concentrically with independent torsional degrees of freedom. While static models of concentric tube robots exist [13], [15], the inertial dynamics of a concentric precurved tube system have never been derived, despite recent experimental characterizations [26]. In this paper, we work out the implications of the concentric-tube kinematic constraints in a dynamic context for the first time. The model accommodates any number of tubes with arbitrary pre-curvature functions and external

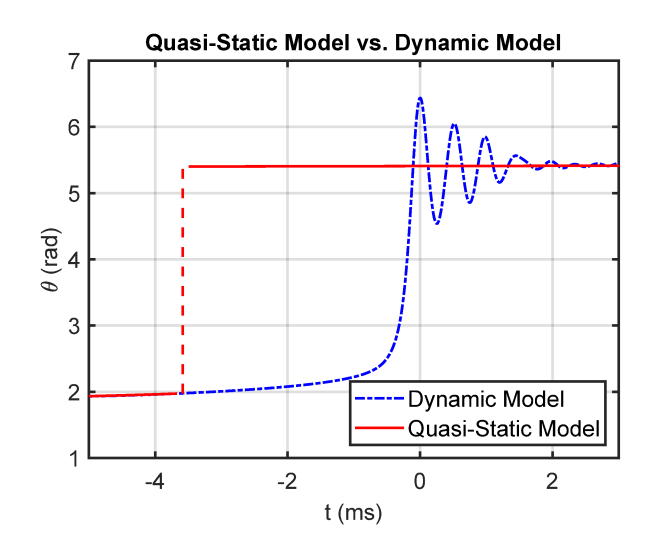


Fig. 2. A quasi-static model is incapable of properly tracking the trajectory of a CTR when transitioning through an elastic snap. The behavior is incorrectly resolved as an instantaneous jump discontinuity, and convergence is difficult across the discontinuity. In contrast, the dynamic model predicts the smooth transition across the unstable point and the following oscillations.

loading and considers the dynamic effects of tube inertia (both linear and rotational), material damping, Coulomb and viscous friction, and the inertia of a rigid body held at the robot's tip. We validate the model with experiments measuring the dynamic behavior of the device during an elastic instability, (as illustrated graphically in Figure 1) and also during tissue grasping.

II. DERIVATION OF CONCENTRIC TUBE PDES

Following the Cosserat rod model in [37], a tube or rod with negligible shear and extension (i.e. a Kirchhoff rod) is governed by the following set of nonlinear, hyperbolic, partial differential equations [15],

$$\begin{aligned}
\boldsymbol{p}_{i,s} &= \boldsymbol{R}_{i}\boldsymbol{e}_{3}, & \boldsymbol{p}_{i,t} &= \boldsymbol{R}_{i}\boldsymbol{q}_{i} \\
\boldsymbol{R}_{i,s} &= \boldsymbol{R}_{i}\widehat{\boldsymbol{u}}_{i}, & \boldsymbol{R}_{i,t} &= \boldsymbol{R}_{i}\widehat{\boldsymbol{\omega}}_{i} \\
\boldsymbol{n}_{i,s} &= \rho_{i}A_{i}\boldsymbol{p}_{i,tt} - \boldsymbol{f}_{i} &= \rho_{i}A_{i}\boldsymbol{R}_{i}\left(\widehat{\boldsymbol{\omega}}_{i}\boldsymbol{q}_{i} + \boldsymbol{q}_{i,t}\right) - \boldsymbol{f}_{i} \\
\boldsymbol{m}_{i,s} &= \rho_{i}\boldsymbol{R}_{i}\left(\widehat{\boldsymbol{\omega}}_{i}\boldsymbol{J}_{i}\boldsymbol{\omega}_{i} + \boldsymbol{J}_{i}\boldsymbol{\omega}_{i,t}\right) - \widehat{\boldsymbol{p}}_{i,s}\boldsymbol{n}_{i} - \boldsymbol{l}_{i} \\
\boldsymbol{q}_{i,s} &= -\widehat{\boldsymbol{u}}_{i}\boldsymbol{q}_{i} + \widehat{\boldsymbol{\omega}}_{i}\boldsymbol{e}_{3} \\
\boldsymbol{\omega}_{i,s} &= \boldsymbol{u}_{i,t} - \widehat{\boldsymbol{u}}_{i}\boldsymbol{\omega}_{i},
\end{aligned} \tag{1}$$

where all variables are functions of time t and reference arc length s, and additional constitutive laws are used to relate the internal forces to the kinematic variables. Note that throughout the paper, we will follow the standard PDE notational convention of using subscripts s and t to denote partial derivatives with respect to s and t respectively (i.e. $p_{i,s} = \frac{\partial p_i}{\partial s}$), while a numerical subscript or i subscript is used to denote a variable belonging to a particular tube in a multitube collection. The physical meanings of all the variables in the equations above are summarized in Table I. The goal of this section is to derive the dynamic equations of motion for concentric tubes by starting from the dynamics of a single

rod (1) and applying the kinematic constraints that enforce multiple tubes to be concentric.

A. Assumptions

For the reader's convenience, we here collect and summarize the assumptions underlying the model presented in this section.

- Assumptions associated with the general Cosserat rod framework: tube cross sections remain planar and maintain their shape during tube deformation.
- Additional assumptions associated with Kirchhoff rods: the tubes cannot stretch axially (inextensible) or shear in transverse directions. This means that the only allowed modes of deformation are bending and torsion.
- Perfect concentricity of tubes is assumed. Thus all tubes share a common centerline and tangent at any arc length.
- Inextensibility and concentricity together imply that any actuator-dictated translations of tube bases are instantly transferred along the length of the tubes.
- We assume that the robot's actuators dictate the position and angle of each tube's base; i.e. we decouple any dynamics associated with the motors or drivetrain and assume the interface at the base of each tube is rigid.
- As explained below, we assume the speed and acceleration of the translational actuators is small enough to be considered quasi-static. This is reasonable because typical actuation bandwidth is much lower than the natural frequencies of the flexible robot structure. Note that the linear velocity of points along the robot are still included with appropriate Coriolis effects arising from the rotating reference frame.
- Frictional energy dissipation is described by a conventional Coulomb-plus-viscous model applied at points where tubes abruptly change curvature or terminate.
- A linear constitutive law is assumed to relate internal moment to the curvature and torsion variables; however, the overall model is still geometrically nonlinear, and a nonlinear material law could easily be accommodated in the framework.

B. arc length Kinematics

Let there be N inextensible tubes. As shown in Figure 3, the arc length parameter s is defined so that $\boldsymbol{p}_i(t,0)=\boldsymbol{0}$ is the fixed location of a constraining baseplate hole through which all tubes pass. An actuator translation β_i is defined so that the global position of the i^{th} tube base is $\begin{bmatrix} 0 & 0 & \beta_i(t) \end{bmatrix}^{\top}$. Note that β_i will be a negative number since the actuators are behind the baseplate. Each tube has a total length of l_i .

Note that our convention of prescribing s=0 at the baseplate means that a particular value of the parameter s will describe different material tube points over time since the tubes can slide in and out of the base plate as they are actuated. This choice departs slightly from a conventional Cosserat rod framework where s would correspond to a material point, but it is consistent with prior concentric-tube robot models and is more convenient for formulating the kinematics. To reduce the complexity of the derivation, we assume the insertion speed

TABLE I NOTATION AND DEFINITIONS

Symbol	Units	Definition	
s	m	Reference arclength	
t	s	Time	
\boldsymbol{p}	m	Global position in Cartesian coordinates	
R	none	Rotation matrix of material orientation	
h	none	Quaternion for the material orientation	
\boldsymbol{n}	N	Internal force in the global frame	
m	Nm	Internal moment in the global frame	
f	N/m	Distributed force in the global frame	
l	Nm/m	Distributed moment in the global frame	
\boldsymbol{u}	1/m	Curvature vector in the local frame	
θ_i	rad	Angle between tube i and tube 1	
$oldsymbol{R}_z(heta_i)$	none	Matrix for rotation by θ_i about z-axis,	
		either $\mathbb{R} \mapsto SO(3)$ or $\mathbb{R} \mapsto SO(2)$	
γ_i	rad/s	Relative angular velocity, $\gamma_i := \theta_{i,t}$	
$oldsymbol{q}$	m/s	Velocity in the local frame	
ω	1/s	Angular velocity in the local frame	
A	m ²	Cross-sectional area	
ρ	kg/m ³	Material density	
J	m^4	Second moment of area tensor	
$oldsymbol{u}^*$	1/m	pre-curvature vector	
		For a straight rod $u^* = 0$.	
\boldsymbol{K}	Nm^2	Stiffness matrix for bending and twisting	
		$\begin{bmatrix} EI_{xx} & 0 & 0 \end{bmatrix}$	
		$\mathbf{K} = \begin{bmatrix} 0 & EI_{yy} & 0 \end{bmatrix}$	
		$\begin{bmatrix} 0 & 0 \end{bmatrix} GI_{zz}$	
E	Pa	Young's modulus	
G	Pa	Shear modulus	
B	Nm ² s	Damping matrix for bending and twisting	
\boldsymbol{g}	m/s ²	Gravitational acceleration vector	
m_i	kg	Point mass at tip of tube i	
\boldsymbol{H}_i	kg m ²	Rigid-body inertia matrix coupled to tip	
		of tube i	
β_i	m	Distance along z-axis from the baseplate	
, -		to actuator i. $\beta_i \leq 0$.	
l_i	m	Length of tube i	
e_3	none	Unit vector; $e_3 = \begin{bmatrix} 0 & 0 & 1 \end{bmatrix}^{T}$	
c_i	1/t	Implicit difference coefficient for a state	
- 6		at $t - i\delta t$	
\boldsymbol{y}	misc.	General ODE state vector	
$(\cdot)^b$		Local-frame representation of variable,	
		e.g. $oldsymbol{n}^b = oldsymbol{R}^ op oldsymbol{n}$	
ħ			
(.)		History dependent part of	
		discretized time derivative,	
		e.g. $oldsymbol{q}_tpprox c_0oldsymbol{q}+\overset{\mathfrak{h}}{oldsymbol{q}}$	
or (⋅)^		Mapping from \mathbb{R}^3 to $\mathfrak{se}(3)$.	
0.1 ()		$\begin{bmatrix} 0 & -u_z & u_y \end{bmatrix}$	
		e.g. $\widehat{\boldsymbol{u}} = \begin{bmatrix} 0 & -u_z & u_y \\ u_z & 0 & -u_x \end{bmatrix}$	
		e.g. $\hat{\boldsymbol{u}} = \begin{bmatrix} 0 & -u_z & u_y \\ u_z & 0 & -u_x \\ -u_y & u_x & 0 \end{bmatrix}$	
() \		$\begin{bmatrix} \omega_y & \omega_x & 0 \end{bmatrix}$	
$(\cdot)^{\vee}$		Mapping from $\mathfrak{se}(3)$ to \mathbb{R}^3 , $\widehat{\boldsymbol{u}}^{\vee} = \boldsymbol{u}$	

and acceleration of the translational actuators are relatively small so that $\beta_{i,t} \approx \beta_{i,tt} \approx 0$. While this assumption is a limitation of our model, it is reasonable in practice for applications in which actuator insertion motions occur at much slower frequencies than the natural frequencies of the flexible robot structure itself. In the case of teleoperation for example, typical human hand motion (and thus actuator motion) would not contain frequency content above 5 Hz [38] and can be low-pass filtered even further if desired, while the vibrations

exhibited in our torsional experiments in this paper occur on the order of 2000 Hz.

The tube indices are ordered so that a larger index corresponds to a larger cross section, i.e. tube 1 is the innermost tube and tube 2 is the second innermost tube. We restrict our attention to configurations where $\beta_i < \beta_j$ and $\beta_i + l_i > \beta_j + l_j$ for i < j so that transition points are always caused by the termination of the outermost tube. The concentric constraint is that all tubes have the same centerline, which is expressed by the equation

$$\mathbf{p}_i(t,s) = \mathbf{p}_1(t,s) \quad \forall s \in [\beta_i \quad \beta_i + l_i].$$
 (2)

This equation may be differentiated with respect to arc length (s) to obtain the constraint that the tube tangents must be aligned

$$R_i e_3 = R_1 e_3. \tag{3}$$

This implies that the tube rotation matrices only differ by a rotation about their common z-axes. Thus we define an angle θ_i such that

$$\mathbf{R}_i = \mathbf{R}_1 \mathbf{R}_z(\theta_i),$$

where

$$\mathbf{R}_z(\theta_i) = \begin{bmatrix} \cos \theta_i & -\sin \theta_i & 0 \\ \sin \theta_i & \cos \theta_i & 0 \\ 0 & 0 & 1 \end{bmatrix}.$$

and $\theta_1=0$ by definition. Substituting this relationship into the definition of the curvature of the i^{th} tube results in

$$\mathbf{u}_i = \left(\mathbf{R}_i^{\top} \mathbf{R}_{i,s}\right)^{\vee} = \mathbf{R}_z^{\top}(\theta_i) \mathbf{u}_1 + \theta_{i,s} \mathbf{e}_3.$$
 (4)

The third component of the above equation defines the arc length derivative of θ_i as the difference between the tube torsional strains:

$$\theta_{i,s} = u_{i,z} - u_{1,z}.$$
 (5)

where the subscript z denotes the third (z-axis) component of a vector expressed in the body frame throughout the paper. The above description of the arc length kinematics is common to the prior static models of concentric tube robots, and more detail can be found in [15].

C. Time Kinematics and Compatibility Equations

Moving into the realm of dynamics, we begin by defining variables to represent various time-derivative quantities. For tube i, at arc length s, the body-frame linear velocity q_i and angular velocity ω_i are defined as

$$oldsymbol{p}_{i,t} = oldsymbol{R}_i oldsymbol{q}_i, ~~ oldsymbol{R}_{i,t} = oldsymbol{R}_i \widehat{oldsymbol{\omega}}_i$$

Comparing the arc length derivatives of the above equations to the time derivatives of the analogous arc length kinematic equations in (1) allows us to derive the following compatibility equations (which are also stated in (1):

$$q_{i,s} = -\widehat{u}_i q_i + \widehat{\omega}_i e_3 \qquad \omega_{i,s} = u_{i,t} - \widehat{u}_i \omega_i,$$
 (6)

The concentric constraint (2) implies that all tubes have the same global linear velocity $p_{i,t}$ and acceleration $p_{i,tt}$.

Analogous to (4), since the tube rotation matrices share the same z-axis, the body-frame angular velocities are related by

$$\boldsymbol{\omega}_i = \left(\boldsymbol{R}_i^{\top} \boldsymbol{R}_{i,t}\right)^{\vee} = \boldsymbol{R}_z^{\top}(\theta_i) \boldsymbol{\omega}_1 + \theta_{i,t} \boldsymbol{e}_3$$
 (7)

the third component of which is

$$\theta_{i,t} = \omega_{i,z} - \omega_{1,z}.$$

For convenience, and to eventually arrive at a first-order system of PDE's, we define a new state variable $\gamma_i := \theta_{i,t}$ (representing the difference between the z-axis angular velocities of tube i and tube 1 such that (8) is written as

$$\boldsymbol{\omega}_i = \boldsymbol{R}_z^{\top}(\theta_i)\boldsymbol{\omega}_1 + \gamma_i \boldsymbol{e}_3. \tag{8}$$

To get the arc length derivative of γ_i , we differentiate (5) with respect to time:

$$\gamma_{i,s} = u_{i,z,t} - u_{1,z,t}. (9)$$

D. Forces and Inertial Dynamics

Next, we consider the dynamic equilibrium of internal forces and moments carried by the tubes. We introduce a variable for the concentric tube robot's total internal force, which is the sum of the global-frame internal force vectors n_i carried by each tube:

$$oldsymbol{n} := \sum_{i=1}^N oldsymbol{n}_i.$$

The third line of (1) is obtained by differentiating the conditions of dynamic equilibrium (Newton's second law) and defines the arc length derivative of n_i for each tube, allowing us to re-write n_s as

$$\boldsymbol{n}_s = \sum_{i=1}^N \rho_i A_i \boldsymbol{p}_{i,tt} - \boldsymbol{f}_i,$$

where ρ_i and A_i are the density and cross sectional area of tube i, and f_i is a global external distributed force applied to tube i. The concentric constraint with the assumption of quasistatic actuator motion implies $p_{i,tt} = p_{1,tt}$ (all tubes share the same linear acceleration in the global frame), and we can differentiate the kinematics to find $p_{1,tt} = R_1 \left(\hat{\omega}_1 q_1 + q_{1,t} \right)$ (which is also stated in (1). Thus we can write

$$\boldsymbol{n}_s = -\boldsymbol{f} + \boldsymbol{R}_1 \left(\widehat{\omega}_1 \boldsymbol{q}_1 + \boldsymbol{q}_{1,t} \right) (\rho A), \tag{10}$$

where $(\rho A) := \sum_{i=1}^N \rho_i A_i$ and $\boldsymbol{f} := \sum_{i=1}^N \boldsymbol{f}_i$ is the total external distributed load applied to the robot.

Turning now to moments, we seek a differential equation governing the axial (body-frame z) component of each tube's moment vector (the torsional moment) and an additional equation governing the transverse (body-frame xy) component of the total moment carried by the robot. Defining m_i^b as the internal moment of tube i, expressed in the body-frame of tube i, we have

$$m{m}_i^b = m{R}_i^ op m{m}_i$$
 and $m{m}_{i|s}^b = -\widehat{m{u}}_i m{m}_i^b + m{R}_i^ op m{m}_{i,s}$

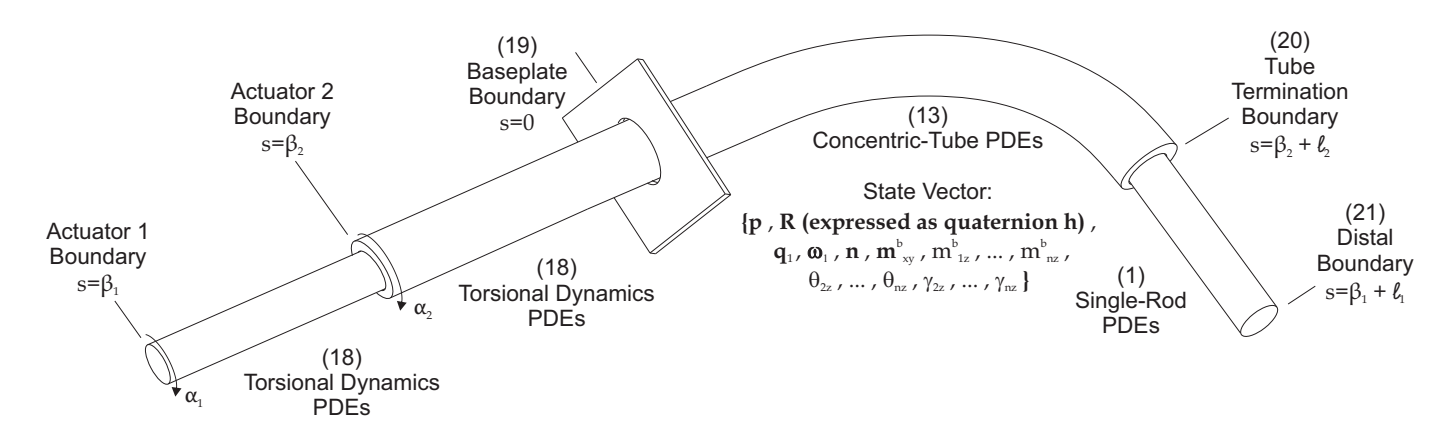


Fig. 3. A concentric tube robot sketch is annotated to describe the PDE boundary value problem. A main contribution of this paper is deriving the equations of motion for a concentric tube collection (13), and a simplified set of PDEs (18) is obtained under the assumption that tubes are held straight below the base.

since $\boldsymbol{R}_{i,s}^{\top} = -\widehat{\boldsymbol{u}}_i \boldsymbol{R}_i^{\top}$. Now substituting in $\boldsymbol{m}_{i,s}$ from (1), selecting only the third (z-axis) component of $\boldsymbol{m}_{i,s}^b$, and neglecting any external distributed moments \boldsymbol{l}_i , we write

$$rac{\partial m_{i,z}}{\partial \mathbf{s}} = -oldsymbol{e}_3^{ op} \widehat{oldsymbol{u}}_i oldsymbol{m}_i^b +
ho_i oldsymbol{e}_3^{ op} \left(\widehat{oldsymbol{\omega}}_i oldsymbol{J}_i oldsymbol{\omega}_i + oldsymbol{J}_i oldsymbol{\omega}_{i,t}
ight),$$

where we have used the properties $\boldsymbol{a}^{\top} \widehat{\boldsymbol{a}} = 0$ and $(\boldsymbol{R}\boldsymbol{a})^{\wedge} = \boldsymbol{R} \widehat{\boldsymbol{a}} \boldsymbol{R}^{\top}$ for $\boldsymbol{a} \in \mathbb{R}^3$ and $\boldsymbol{R} \in \mathrm{SO}(3)$ from [39] to reveal that $\boldsymbol{e}_3^{\top} \boldsymbol{R}_i^{\top} \widehat{\boldsymbol{p}}_{i,s} \boldsymbol{n}_i = \boldsymbol{0}$. Additional simplifications are gained by recognizing that \boldsymbol{J}_i is the second moment of area tensor of the i^{th} tube cross section expressed in the body-frame:

$$m{J}_i = egin{bmatrix} I_{xx,i} & 0 & 0 \ 0 & I_{yy,i} & 0 \ 0 & 0 & I_{zz,i} \end{bmatrix}.$$

The terms in J_i can be calculated for a circular tube with inner diameter ID_i and outer diameter OD_i as

$$I_{xx,i} = I_{yy,i} = \frac{1}{2}I_{zz,i} = I_i = \pi(OD_i^4 - ID_i^4)/64.$$

This then implies $\rho_i e_3^{\top} \hat{\omega}_i J_i \omega_i = \mathbf{0}$ so that using (8) we can write

$$\frac{\partial m_{i,z}}{\partial s} = -\mathbf{e}_{3}^{\top} \widehat{\mathbf{u}}_{i} \mathbf{m}_{i}^{b} + \rho_{i} I_{zz,i} \boldsymbol{\omega}_{i,z,t}
= -\mathbf{e}_{3}^{\top} \widehat{\mathbf{u}}_{i} \mathbf{m}_{i}^{b} + 2\rho_{i} I_{i} \left(\boldsymbol{\omega}_{1,z,t} + \gamma_{i,t} \right)$$
(11)

Finally, to derive equations for the transverse components of the total moment, we first define the concentric tube robot's total internal moment, which is the sum of the global frame internal force vectors m_i carried by each tube:

$$m{m} := \sum_{i=1}^N m{m}_i.$$

Using the fourth line of (1), which is the arc length derivative of a dynamic moment balance on each tube, and again neglecting l_i , we have

$$oldsymbol{m}_s = \sum_{i=1}^N
ho_i oldsymbol{R}_i \left(\widehat{oldsymbol{\omega}}_i oldsymbol{J}_i oldsymbol{\omega}_i + oldsymbol{J}_i oldsymbol{\omega}_{i,t}
ight) - \widehat{oldsymbol{p}}_{i,s} oldsymbol{n}_i.$$

Now define m^b as the total internal moment, written in the body frame of tube 1 (the innermost tube), such that

$$oldsymbol{m}^b = oldsymbol{R}_1^ op oldsymbol{m}$$
 and $oldsymbol{m}_s^b = -\widehat{oldsymbol{u}}_1 oldsymbol{m}^b + oldsymbol{R}_1^ op oldsymbol{m}_s.$

Now rewriting $\hat{p}_{i,s}$ using the concentric constraint (3) we have

$$oldsymbol{\widehat{p}}_{i,s}oldsymbol{n}_i = \left(oldsymbol{R}_ioldsymbol{e}_3
ight)^{\wedge}oldsymbol{n}_i = oldsymbol{R}_1oldsymbol{\widehat{e}}_3oldsymbol{R}_1^{ op}oldsymbol{n}_i.$$

Using this we rewrite m_s^b as

$$egin{aligned} m{m}_s^b &= - \, \widehat{m{u}}_1 m{m}^b - \widehat{m{e}}_3 m{R}_1^ op m{n} \ &+ \sum_{i=1}^N
ho_i m{R}_z(heta_i) \left[\widehat{m{\omega}}_i m{J}_i m{\omega}_i + m{J}_i m{\omega}_{i,t}
ight]. \end{aligned}$$

The terms in the summation are simplified again because the structure of J_i for circular tubes implies $R_z(\theta_i)J_i = J_iR_z(\theta_i)$, and the product product $\widehat{\omega}_iJ_i\omega_i$ simplifies to

$$\widehat{\boldsymbol{\omega}}_i \rho_i \begin{bmatrix} I_i & 0 & 0 \\ 0 & I_i & 0 \\ 0 & 0 & 2I_i \end{bmatrix} \boldsymbol{\omega}_i = \rho_i I_i \boldsymbol{\omega}_{i,z} \begin{bmatrix} \boldsymbol{\omega}_{i,y} \\ -\boldsymbol{\omega}_{i,x} \\ 0 \end{bmatrix}.$$

After a few more algebraic steps, we can finally extract the x and y components of m_s^b as

$$\frac{\partial \boldsymbol{m}_{xy}^{b}}{\partial s} = \left\{ -\widehat{\boldsymbol{u}}_{1} \boldsymbol{m}^{b} - \widehat{\boldsymbol{e}}_{3} \boldsymbol{R}_{1}^{\top} \boldsymbol{n} + (\rho I) \boldsymbol{\omega}_{1,t} \right\}_{xy} + \begin{bmatrix} \omega_{1,y} \\ -\omega_{1,x} \end{bmatrix} \sum_{i=1}^{N} \rho_{i} I_{i}(\omega_{1,z} + \gamma_{i}), \tag{12}$$

where $(\rho I) = \sum_{i=1}^{N} \rho_i I_i$.

E. Summary of Concentric-Tube PDEs

Pulling together all the results in this section, we can succinctly state the set of PDEs for a concentric-tube system in the form of a first-order vector system

$$\boldsymbol{y}_{s}=\boldsymbol{f}\left(\boldsymbol{y},\boldsymbol{y}_{t}\right),$$

where the state vector \boldsymbol{y} contains state variables \boldsymbol{p} , \boldsymbol{R} , \boldsymbol{q} , $\boldsymbol{\omega}$, \boldsymbol{n} , \boldsymbol{m}_{xy}^b , $m_{1,z}^b$, and $m_{i,z}^b$, θ_i , and γ_i for $i \in [2\ N]$, as shown

in Figure (3). The full system can be summarized:

$$p_{s} = R_{1}e_{3}$$

$$R_{1,s} = R_{1}\hat{u}_{1},$$

$$q_{1,s} = -\hat{u}_{1}q_{1} + \hat{\omega}_{1}e_{3}$$

$$\omega_{1,s} = u_{1,t} - \hat{u}_{1}\omega_{1}$$

$$n_{s} = -f + R_{1}\left(\hat{\omega}_{1}q_{1} + q_{1,t}\right)\left(\rho A\right)$$

$$\frac{\partial m_{xy}^{b}}{\partial s} = \left\{-\hat{u}_{1}m^{b} - \hat{e}_{3}R_{1}^{\top}n + (\rho I)\omega_{1,t}\right\}_{xy}$$

$$+ \begin{bmatrix}\omega_{1,y}\\-\omega_{1,x}\end{bmatrix}\left((\rho I)\omega_{1,z} + \sum_{i=1}^{N}\rho_{i}I_{i}\gamma_{i}\right)$$

$$\frac{\partial m_{i,z}^{b}}{\partial s} = -e_{3}^{\top}\hat{u}_{i}m_{i}^{b} + 2\rho_{i}I_{i}\left(\omega_{1,z,t} + \gamma_{i,t}\right)$$

$$\theta_{i,s} = u_{i,z} - u_{1,z}$$

$$\gamma_{i,s} = u_{i,z,t} - u_{1,z,t}.$$
(13)

This system is analogous to the classical PDE's for a single-rod in (1), but it accounts for multiple concentric tubes. The system also represents a dynamic generalization of well-established static models for concentric-tube robots [13], [14], [15]. Simply setting all velocity-associated variables to zero recovers the conventional static model. Thus, this model's prediction of snapping points will be identical to those predicted by the static models in [24], [25], but the dynamics model can provide additional information to characterize the motions of the robot during the snap transition itself. Note that like these previous static models, this model can incorporate arbitrary precurved tube shapes and different numbers of segments. Boundary conditions at segment transitions are discussed in Section III-C.

Note that it is possible to choose a different set of state variables in which to express this model, such as the body-frame curvature components instead of the global-frame moment components [15], but one advantage of the choice made here is that the total internal moment is continuous along the robot length, which simplifies numerical integration across transitions in pre-curvature or the end of a tube.

As in (1), in order to solve the PDE system (13), we will need to implement a specific constitutive stress-strain law, as well as a strategy for numerical discretization and solution of the resulting discretized equations. These two additions are developed together in the next section.

III. NUMERICAL SOLUTION OF CONCENTRIC-TUBE PDES

In this section we discuss the details of numerical solution of the concentric-tube PDEs stated in (13) subject to a specific constitutive law.

A. Constitutive Laws

To obtain a complete set of equations for the dynamics of a concentric-tube system, we must postulate a material constitutive law that relates the kinematic variables u_i to the

body-frame internal moments m_i . We adopt a linear viscoelastic law with material damping [40] such that

$$\boldsymbol{m}_{i}^{b} = \boldsymbol{K}_{i}(\boldsymbol{u}_{i} - \boldsymbol{u}_{i}^{*}) + \boldsymbol{B}_{i}\boldsymbol{u}_{i\,t}, \tag{14}$$

where

$$\boldsymbol{K}_i = \begin{bmatrix} E_i & 0 & 0 \\ 0 & E_i & 0 \\ 0 & 0 & G_i \end{bmatrix} \boldsymbol{J}_i,$$

and B_i is a damping coefficient matrix with axisymmetric diagonal coefficients, that is

$$\boldsymbol{B}_{i} = \begin{bmatrix} B_{B,i} & 0 & 0 \\ 0 & B_{B,i} & 0 \\ 0 & 0 & B_{T,i} \end{bmatrix}.$$

The total internal moment in the tube 1 body frame is then expressed as

$$oldsymbol{m}^b = \sum_{i=1}^N oldsymbol{R}_z(heta_i) \left[oldsymbol{K}_i(oldsymbol{u}_i - oldsymbol{u}_i^*) + oldsymbol{B}_i oldsymbol{u}_{i,t}
ight].$$

Note that this is a differential equation in u_i , which was not originally included as a state variable; however, the time discretization strategy in the next section converts this viscoelastic constitutive law into an algebraic equation which allows us to compute u_i from existing state variables.

B. Implicit Time Discretization

It is well known that conventional *explicit* integration routines (e.g. Forward Euler or explicit Runge-Kutta methods) in time perform poorly for systems with stiff dynamics because the Courant-Friedrichs-Lewy (CFL) condition limits the maximum time step that can be stably executed [41]. To avoid this limitation, we adopt a fully implicit method to discretize the time derivatives [42]. This creates an ordinary differential equation, in the arc length variable *s*, which can be solved at each time step subject to boundary conditions at the proximal and distal ends of the robot, following [35], [36], [43], [44], [45]. The structure of the spatial boundary value problem thus created is similar to conventional static models (e.g. [13], [15]) and can be solved by similar methods such as shooting, finite-difference, or finite-element methods, as we discuss in Section III-F.

Many implicit finite difference schemes, such as the backward Euler, BDF-2, trapezoidal rule, and BDF- α [46] methods, fit the form

$$\boldsymbol{y}_{t}(t_{i}) \approx c_{0}\boldsymbol{y}(t_{i}) + \sum_{j=1}^{\infty} c_{j}\boldsymbol{y}(t_{i-j}) + d_{j}\boldsymbol{y}_{t}(t_{i-j}).$$
 (15)

For example, for a discrete time step of Δt , backward Euler has $c_0 = \Delta t^{-1}$, $c_1 = -\Delta t^{-1}$, $c_j = 0 \ \forall j > 1$, and $d_j = 0 \ \forall j$. We can abstract the details of the specific scheme by using a single variable to represent all history dependent terms, that is

$$\boldsymbol{y}_t(t_i) \approx c_0 \boldsymbol{y}(t_i) + \boldsymbol{\dot{y}}(t_i).$$

Applying such an implicit discretization to the differential equation, defined by our constitutive law, allows us to solve for each tube's independent $u_{i,z}$ in terms of its torsional moment $m_{i,z}$

$$u_{i,z} = \frac{m_{i,z}^b + G_i J_i u_{i,z}^* - B_{i,z} \dot{u}_{i,z}}{G_i J_i + c_0 B_{i,z}}.$$
 (16)

Applying the discretization to the total internal moment, we obtain

$$oldsymbol{m}^b = \sum_{i=1}^N oldsymbol{R}_z(heta_i) \left[oldsymbol{K}_i (oldsymbol{u}_i - oldsymbol{u}_i^*) + oldsymbol{B}_i (c_0 oldsymbol{u}_i + oldsymbol{\dot{u}}_i)
ight].$$

We can then apply (4) and solve for $u_{1,xy}$ as

$$u_{1,xy} = \frac{m_{xy}^b - B_{xy} u_{1,xy}^b + \sum_{i=1}^N R_z(\theta_i) E_i I_i u_{i,xy}^*}{\sum_{i=1}^N E_i I_i + c_0 B_{i,xy}}, \quad (17)$$

where $B_{xy} = \sum_{i=1}^{N} B_{i,xy}$ and we have overloaded the symbol $\mathbf{R}_z(\theta_i)$ to include its 2×2 version, understood by context.

Replacing all time derivatives on the right hand side of the PDEs in (13) with the discretization in (15), effectively converts the PDEs into a set of ODEs, in arc length, of the form

$$\boldsymbol{y}_{s} = \boldsymbol{f}(\boldsymbol{y}).$$

All terms on the right hand side of (13) can now be computed from existing state variables through the algebraic equations (16), (17), (4), and (14).

C. Boundary Conditions

The inputs to the robot are the actuator positions $\beta_i(t)$ and angles α_i . Below the base we assume the tubes are held straight, which results in simplifications to the equations of motion. We use an absolute angle ψ_i to describe the rotation of each tube below the base. The PDE system describing angular rotation and torque is

$$\psi_{i,s} = u_{i,z}$$

$$\psi_{i,ts} = u_{i,z,t}$$

$$m_{i,z,s}^b = (\rho I_{zz})_i \psi_{i,tt},$$
(18)

where $u_{i,z}$ is calculated as previously described. There is an unknown reaction torque on each actuator $m_{i,z}(t,\beta_i)$. At the base, there is an unknown reaction force $\boldsymbol{n}(t,0)$ and transverse moment $\boldsymbol{m}_{xy}(t,0)$. The baseplate is stationary and arbitrarily defined at the origin so that $\boldsymbol{p}(t,0)=\boldsymbol{q}(t,0)=\boldsymbol{0}$. While we have neglected insertion speed, we still account for the axial angular velocity of the tube bases – only the transverse angular velocities are zero at the base, $\boldsymbol{\omega}_{1,xy}(t,0)=\boldsymbol{0}$. The main system is coupled to the system below the base so that

$$\mathbf{R}_{1}(t,0) = \mathbf{R}_{z}[\psi_{1}(t,0)]
\omega_{1,z}(t,0) = \psi_{1,t}(t,0)
\theta_{i}(t,0) = \psi_{i}(t,0) - \psi_{1}(t,0)
\gamma_{i}(t,0) = \psi_{i,t}(t,0) - \psi_{1,t}(t,0).$$
(19)

At distal tube ends, we can use boundary conditions to prescribe external point forces and moments as well as coupling to the rigid body dynamics of external objects the robot is manipulating. For example, suppose that at the end of tube i ($s = \beta_i + l_i$) the tube is subjected to an external force F and moment M and coupled to a rigid body with mass m_i and mass moment of inertia H_i :

$$m{H}_i = egin{bmatrix} H_{i,xx} & 0 & 0 \\ 0 & H_{i,yy} & 0 \\ 0 & 0 & H_{i,zz} \end{bmatrix}.$$

A force and moment balance on the attached rigid body in the body frame of tube 1 then gives

$$F(t,s) + n(t,s^{+}) - n(t,s^{-}) = m_i p_{tt}$$
 (20)

$$\boldsymbol{M}_{xy}^b(s) + \boldsymbol{m}_{xy}^b(s^+) - \boldsymbol{m}_{xy}^b(s^-) = \left(\boldsymbol{H}_i \bar{\boldsymbol{\omega}}_{i,t} + \widehat{\boldsymbol{\omega}}_i \boldsymbol{H}_i \bar{\boldsymbol{\omega}}_i,\right)_{xy}$$

$$M_z(t) - m_{i,z}^b(t, \beta_i + l_i) = H_{i,zz}\omega_{i,z,t},$$

where for convenience we have defined $\bar{\omega}_i := R_z^T(\theta_i)\omega_i$. The termination of the final tube requires the entire distal wrench be balanced, that is

$$F(t) - n(t, \beta_1 + l_1) = m_1 p_{tt}$$

$$M^b(t) - m^b(t, \beta_1 + l_1) = H_1 \omega_t + \widehat{\omega} H_1 \omega.$$
(21)

D. Modeling Friction

In static models for concentric-tube robots, friction has usually been neglected; however, some efforts have been made to describe the frictional torque between tubes using a Coulomb friction model [22], [23]. For our initial investigation into friction in dynamic CTR models, we follow the approach in [22] which modeled friction as a set of point torques at locations where the precurvature is discontinuous or where a tube leaves another tube (i.e. wherever the internal moment is discontinuous). Lumping all friction into point moments at these discontinuities is justified in [22] by the observation that as the clearance between tubes becomes small, the distributed normal force between the tubes can be approximated by a pair of large point forces separated by a small axial distance at points of curvature discontinuity or the end of a tube. When a conventional Coulomb friction model is applied, the axial distance gets absorbed into the unknown frictional coefficient, so that the friction moment is proportional to the magnitude of the discontinuity in internal moment.

For generality, we also include a standard viscous damping term in addition to Coulomb (sliding) friction. If an internal moment discontinuity occurs at arc length s, the total dissipative torque between tube 1 and tube 2 is then given by

$$\tau_f(s) = \mu' \|\Delta \mathbf{m}_{1,xy}^b(s)\| \operatorname{sig}(\gamma_2(s)) + \nu \gamma_2(s),$$
 (22)

where $\Delta \boldsymbol{m}_{1,xy}^b(s) := \boldsymbol{m}_{1,xy}^b(s^+) - \boldsymbol{m}_{1,xy}^b(s^-)$ is the discontinuous change in the internal moment of tube 1 at $s, \ \mu'$ is the generalized friction coefficient as described in [22], ν is a viscous friction coefficient, and "sig" is a sigmoid function $\operatorname{sig}(\gamma) = \gamma/\sqrt{\gamma^2 + \epsilon^2}$ which is approximately equal to the sign of γ but is continuous at $\gamma = 0$. Note that ϵ should be chosen to be smaller than the typical tube angular velocities expected to be seen in the system. The friction torque between

tube 1 and tube 2 is then applied to each tube in opposite directions leading to the following transition conditions at s:

$$m_{1,z}^b(s^+) = m_{1,z}^b(s^-) - \tau_f$$

 $m_{2,z}^b(s^+) = m_{2,z}^b(s^-) + \tau_f.$ (23)

To apply friction at the point where the outer tube terminates, the boundary condition in (20) is re-written as

$$M_z(t) - m_{2,z}^b(t, \beta_2 + l_2) - \tau_f = H_{2,zz}\omega_{2,z,t}$$

$$m_{1,z}^b((\beta_2 + l_2)^+) = m_{1,z}^b((\beta_2 + l_2)^-) - \tau_f.$$

Friction also occurs at the point where the outer tube passes through a hole in the base plate (see Figure 3). This introduces another frictional torque on the outer tube, given by

$$\tau_{base} = \mu'_{base} \| \mathbf{m}_{xy}^b(0) \| \operatorname{sig}(\omega_{2z}(0)) + \nu_{base}\omega_{2z}(0)$$

$$m_{2,z}^b(0^+) = m_{2,z}^b(0^-) + \tau_f(0) + \tau_{base}.$$
(24)

Note that frictional forces between the tubes may also be present in the axial direction. While these forces are significant, they do not significantly affect the robot shape because of the axial stiffness of the tubes and their concentric constraints. No shape hysteresis is observed when translating the tubes relative to one another.

E. Orientation as Quaternions

We have used rotation matrices in our model development, but in our numerical implementation, we represent orientation using non-unit quaternions as in [47] to avoid degradation of orthogonality in the rotation matrices due to numerical approximation. Our quaternion follows the convention $h := h_0 + h_1 i + h_2 j + h_3 k$. Rather than the differential equation for \mathbf{R}_s , we now have an equation

$$m{h}_s = rac{1}{2} egin{bmatrix} 0 & -u_1 & -u_2 & -u_3 \ u_1 & 0 & u_3 & -u_2 \ u_2 & -u_3 & 0 & u_1 \ u_3 & u_2 & -u_1 & 0 \end{bmatrix} m{h}.$$

The orientation at the base is now given by

$$\boldsymbol{h}(t,0) = \begin{bmatrix} \cos\left(\frac{1}{2}\psi_1(t,0)\right) & 0 & \sin\left(\frac{1}{2}\psi_1(t,0)\right) \end{bmatrix}^{\top}.$$

Other calculations involving R can be left unchanged, and the orthonormal rotation matrix is obtained from the quaternion by

F. Spatial BVP Solution

Applying the above semi-discretization in time creates a set of ordinary differential equations in s with boundary conditions at both ends. In the continuum robot literature, shooting methods are often used to solve such problems efficiently (e.g. in statics models, [10] and our prior dynamics work [35], [36]). This approach is efficient because the computational effort grows only linearly with the spatial resolution, and we employ shooting in our experimental validation of robot vibrations during tissue grasping in Section V. To describe the

fast torsional dynamics of the snap-through motion (occurring over an interval of about 1ms [26]), we need to take very small time steps, and the shooting problem becomes numerically sensitive. Thus, for the snapping experiments in Section IV, we use a finite difference strategy to solve the BVP in s as described below.

Consider a general state variable $\bar{\boldsymbol{y}}(s) \in \mathbb{R}^M$ with an ODE $\bar{\boldsymbol{y}}_s = f(s, \bar{\boldsymbol{y}})$. Let the domain be discretized into N grid points s_1 through s_N , and let the approximate state at these points be denoted by $\boldsymbol{y}_i := \boldsymbol{y}(s_i)$. Using the midpoint rule one can write a finite difference equation

$$\frac{\mathbf{y}_{i+1} - \mathbf{y}_i}{s_{i+1} - s_i} \approx f(\frac{s_i + s_{i+1}}{2}, \frac{\mathbf{y}_i + \mathbf{y}_{i+1}}{2}).$$

Let the states over the whole grid be joined in a state vector defined as $\boldsymbol{Y} = \begin{bmatrix} \boldsymbol{y}_1^\top & \boldsymbol{y}_2^\top & \dots & \boldsymbol{y}_N^\top \end{bmatrix}^\top$, then a vector containing the residual errors of the differential equations may be expressed as

$$E(Y) = \begin{bmatrix} \frac{y_2 - y_1}{s_2 - s_1} - f(\frac{s_1 + s_2}{2}, \frac{y_1 + y_2}{2}) \\ \frac{y_3 - y_2}{s_3 - s_2} - f(\frac{s_2 + s_3}{2}, \frac{y_2 + y_3}{2}) \\ \vdots \\ \frac{y_N - y_{N-1}}{s_N - s_{N-1}} - f(\frac{s_{N-1} + s_N}{2}, \frac{y_{N-1} + y_N}{2}) \end{bmatrix}. \quad (25)$$

The boundary conditions are strongly satisfied so that some elements of *u* are specified. Note that the concentric tube problem involves the concatenation of systems (1), (13), and (18), as shown in Figure 3. We use a Levenberg-Marquardt algorithm to solve the nonlinear system so that $\|\mathbf{E}\|^2 < 10^{-9}$, using standard SI units for all variables. The time discretization is implemented using BDF2 [48] which, in the context of (15), has non-zero coefficients $c_0 = 3/(2\Delta t)$, $c_1 = -2/\Delta t$, and $c_2 = 1/(2\Delta t)$. The Jacobian of the above system is sparse (in fact, tridiagonal), so we use sparse matrix data structures and sparse linear solving routines implemented in C++ using the matrix library Eigen [49]. The Jacobian is calculated by first order finite differences with appropriately chosen increments for the magnitudes of the variables. Note that the accuracy of this Jacobian approximation does not affect the accuracy of the model, only the convergence of the iterative solution.

IV. SIMULATION AND EXPERIMENTAL VERIFICATION OF THE SNAPPING PHENOMENON

To illuminate the discussion here and facilitate future work, an example simulation of a snap-through bifurcation is provided at codeocean.com/capsule/1121798. Our experimental setup (Figure 5) consists of a two-tube robot with the outer tube rigidly attached to the baseplate as shown in Figure 4. A Phantom® v310 high-speed camera (Vision Research, Inc., Wayne, NJ, USA) was used to study the robot as it was actuated through an elastic instability, followed by oscillations. The high-speed camera collected data at 50,000FPS ($\Delta t = 20~\mu s$) with a resolution of 256x128 pixels. Disk-shaped markers were affixed to each tube at its tip, so that the relative angle, θ_f between the tubes, could be easily reconstructed from video data.

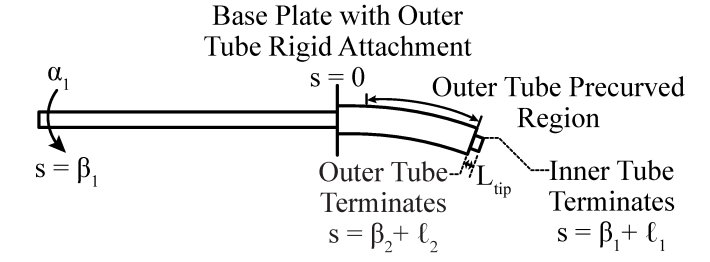


Fig. 4. The validation was performed using a two-tube robot as in [26]. The outer tube was rigidly attached to the baseplate, and the inner tube was rotated at a distance from the baseplate β_1 which is constant for any given trial and varied between trials.

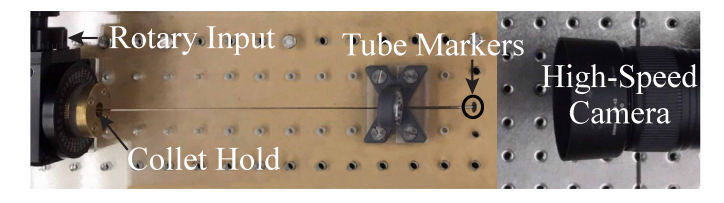


Fig. 5. The experimental setup is shown. The snapping bifurcation was captured on a high-speed camera. Tube markers were affixed to the tip of each tube allowing the relative angle θ_f to be visually reconstructed.

We assume roll and pitch of the tip are negligible so that θ_f is calculated assuming the markers are parallel to the camera plane, which is a reasonable assumption based on the model solution for tip orientation.

A. Measured and Approximate Parameters

The CTR tubes used in these experiments are shown in Fig. 6. The inner tube was made from Nitinol and the outer from stainless steel. The tubes have precurved sections of constant curvature. The precurved section of the outer tube extends all the way to its tip, while the inner tube has a short straight segment at the tip after the precurved section. The precurvature functions were fit from images of the tubes. A description of parameters and their measured, calibrated, or known values is given in Table II. Because the inner tube properties can have a significant effect on the dynamic response, the Young's modulus was experimentally calibrated

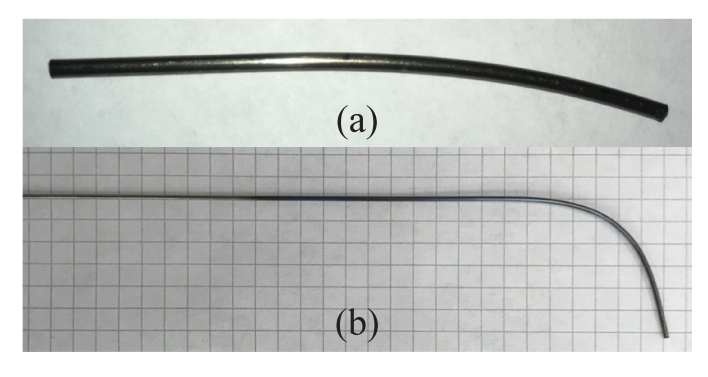


Fig. 6. Component tubes used for two tube robot in validation study before assembly. (a) outer stainless steel tube. (b) inner Nitinol tube (which is a solid circular rod).

TABLE II Model Parameters for Snapping Experiment

NAME	DESCRIPTION	METHOD	VALUE
$r_{i,1}$	Inner radius	Data Sheet	0 mm
$r_{o,1}$	Outer radius	Data Sheet	0.508 mm
$\boldsymbol{E_1}$	Young's modulus	Deflection test	81.97 GPa
ρ_1	Density	Mass/Volume	6493 kg/m ³
$\boldsymbol{\beta}_1$	Exp. 1 location of actuator	Chosen	-112.0 mm
β_1	Exp. 2 location of actuator	Chosen	-162.8 mm
$\boldsymbol{\beta}_1$	Exp. 3 location of actuator	Chosen	-213.6 mm
L_{1S}	Exp. 1 Initial straight length	Fit from image	121.1 mm
L_{1S}	Exp. 2 Initial straight length	Fit from image	171.9 mm
L_{1S}	Exp. 3 Initial straight length	Fit from image	222.7 mm
L_{1C}	Length of curved section	Fit from image	34 mm
$L_{1S,TIP}$	Straight length to tip	Fit from image	12 mm
$u_{1,x}^*$	Precurvature	Fit from image	38.8 m ⁻¹
$r_{i,2}$	Inner radius	Data Sheet	0.62 mm
$r_{o,2}$	Outer radius	Data Sheet	1.055 mm
$\boldsymbol{E_2}$	Young's modulus	Data Sheet	210 GPa
$ ho_2$	Density	Data Sheet	8000 kg/m^3
$\boldsymbol{\beta}_2$	Location of actuator	Fixed to base	0 mm
L_{2S}	Initial straight length	Fit from image	8.1 mm
L_{2C}	Length of curved section	Fit from image	45 mm
$u_{2,x}^*$	Precurvature	Fit from image	8.7 m ⁻¹
m_1	Marker 1 mass	Measured	0.0278 g
$r_{M,1}$	Marker 1 radius	Measured	2.73 mm
$t_{M,1}$	Marker 1 thickness	Measured	1.13 mm
m_2	Marker 2 mass	Measured	0.0714 g
$r_{M,2}$	Marker 2 radius	Measured	4.46 mm
$t_{M,2}$	Marker 2 thickness	Measured	1.09 mm
m_G	Glue mass	Measured	0.02 g
\boldsymbol{B}_*	All mat. damping coeffs	Chosen	0 Nm ² s
ν	Vicious friction coeff	Calibrated	$1.16 \times 10^{-7} \frac{(N-m)s}{rad}$
μ'	Coulomb friction coeff	Calibrated	0.00323
ε	Sigmoid Parameter	Chosen	250 rad/s

in a separate static cantilever deflection test. The density was determined by dividing the measured tube mass by the volume calculated from the tube dimensions.

Preliminary simulation results showed that the inertia of the tracking markers attached to the tube tips was not negligible, so we modeled the markers by implementing the rigid body coupling boundary conditions described in our model equations above. The markers were circular disks with holes to fit around the tubes, so that the inertia components are given by

$$H_{i,xx} = H_{i,yy} = m_i (3(r_{M,i}^2 + r_{o,i}^2) + t_{M,i}^2)/12$$

$$H_{i,zz} = m_i (r_{M,i}^2 + r_{o,i}^2)/2,$$

where $r_{M,i}$ is the marker outer radius, $r_{o,i}$ is the tube outer radius which is also the marker inner radius, and $t_{M,i}$ is the marker thickness. Super glue was used to attach the markers to the tubes. Weighing a single drop to be 0.02 g, we added this amount to each marker mass.

The simulation time step is $\Delta t=10~\mu s$. While our overall approach is capable of running stably at large time steps and capturing slower bending dynamics at real-time rates [35] (as we show in the next section), the small time steps required to resolve the detailed torsional elastic instability dynamics entail non-real-time simulation speeds.

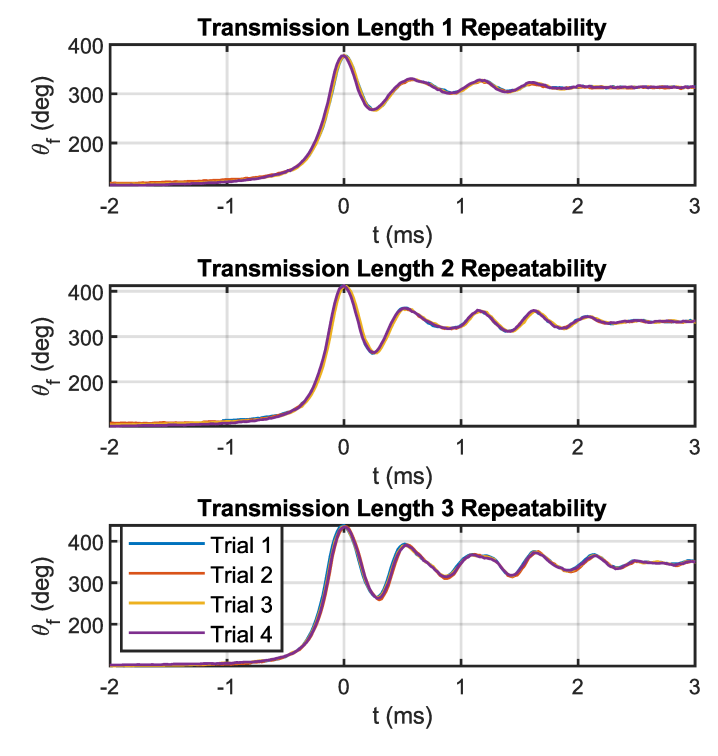


Fig. 7. Each transmission length was tested in four trials to ensure that the robot motion was repeatable. Each of the four trials is plotted simultaneously in the three plots above. The responses are visually identical on a millisecond time scale.

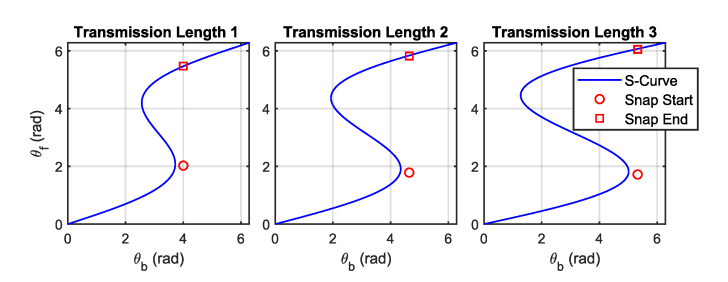


Fig. 8. The base actuation angle was recorded for each trial, and the steady-state tip angles before and after snapping are extracted from the data. Simulated "S-curves" are compared with the experimental behavior. The S-curves pass to the left of the observed initial snapping angles, which is likely due to friction.

B. Experimental Protocol

Experimental validation of this simulation consisted of actuating a concentric-tube robot through an elastic instability transition. This was preformed for three different robot setups where the initial straight length of the inner tube L_{1s} (transmission length) was varied and the overlapping region of the outer and inner tube curvatures was kept the same. Increasing this transmission length also increases the potential of the robot to store elastic energy, resulting in a more forceful bifurcation [26]. The transmission lengths and the actuator locations for the three experimental configurations can be viewed in Table II.

In each configuration, the inner tube tip was extended L_{tip} = 2mm out of the outer tube. The rotary dial was slowly

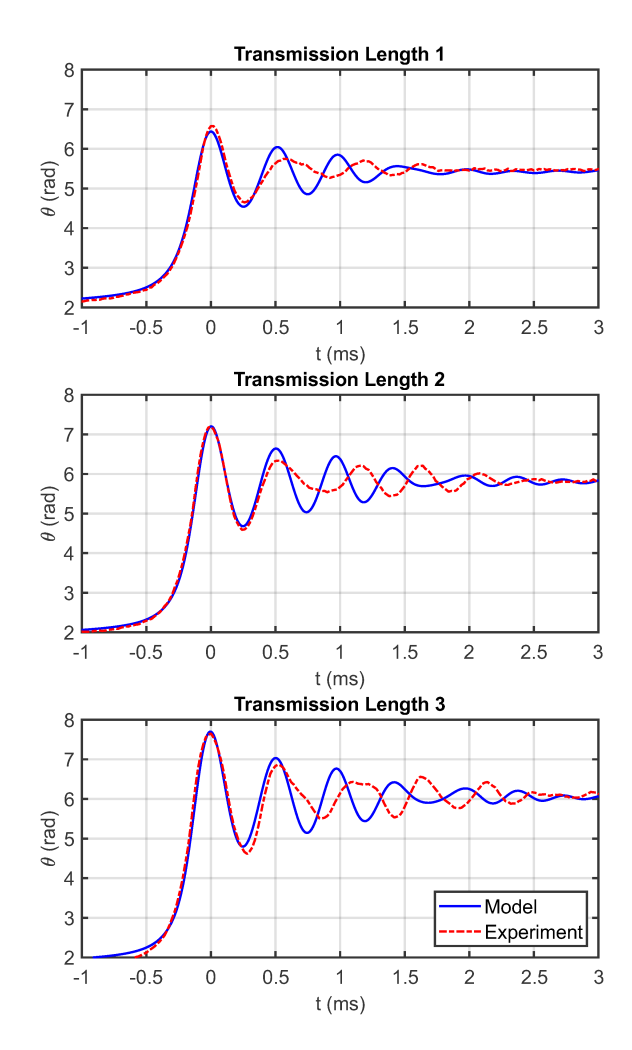


Fig. 9. The model-predicted tip angle is compared with the experimentally observed tip angle using a calibrated Coulomb and viscous friction coefficients.

rotated by hand to induce an elastic instability and video was collected at 50,000 frames per second. To verify repeatability of the data with this procedure, we conducted 4 trials for each transmission length configuration. A comparison of every outcome is overlaid in Figure 7, illustrating that the dynamics introduced by this procedure are highly repeatable and are invariant to very small changes in initial conditions.

C. Calibration and Results

We first verify the static robot parameters by comparing the experimental snap angles to the well-known CTR "Scurve", Figure 8, which uses the static model solution to express the relationship between the relative base angle θ_b and the tip angle θ_f between the tubes [13]. The majority of the model parameters were either read from data sheets, measured directly, or determined from a separate experiment. The Coulomb and viscous friction coefficients are more difficult to directly measure, so μ' and ν were calibrated to the first experimental data set (Transmission Length 1) and subsequently tested on the other two data sets. Since the outer

tube was rigidly fixed to the base plate instead of passing through a hole, friction at the base plate (24) is not present. We performed a least-squares fit of the model prediction to the experimental data, using the height of the first peak, first trough, and final peak of the data set. The sigmoid parameter " ϵ " was chosen to be 250 rad/s since typical angular velocities seen in this system are on the order of 8000 rad/s. All material damping parameters were assigned a value of zero because, according to the data for Nitinol in [50], we calculated that material damping could be responsible for an amplitude decay rate of approximately 1% per cycle. Since the experimental data shows a much larger decay rate than this, the dissipation is probably dominated by frictional effects instead; however, we note that material damping could be significant for non-metal concentric-tube robots, such as those made by 3D printing [2].

The calibrated parameters are listed in Table II, and the resulting model solution for θ_f is compared to the experimental data sets in Figure 9. Note that we synchronized camera time with simulation time by setting the time datum t = 0 at the location of the first peak. The results show that the dynamic model predicts the main features of the experimental data set reasonably well, especially the rise curve when the tube is transitioning through the snap. The overshoot behavior, period of vibration, and subsequent peak heights are also captured well, although an unknown effect around 1 ms creates an abnormally long period in the data, which then creates a phase shift in subsequent data. Applying a Fast Fourier Transform on the experimental data reveals two dominant frequencies (averaging 1.82 MHz and 2.56 MHz) for all three data sets, while the model solution possesses a single dominant frequency of 1.93 MHz. Thus, the model is appropriately capturing the dominant modal behavior present in the experiments. Although significantly more testing and modeling would be necessary to discover why the 2.56 MHz frequency content is missing from the simulation, possible reasons include tube clearance effects, nonlinear friction, and unmodeled dynamics of the interfaces at the tube bases and the actuator drivetrains.

V. APPLICATION TO TISSUE MANIPULATION

In addition to the high-speed snap dynamics validated in the previous section, we also tested the model's ability to describe slower bending dynamics that could potentially arise in scenarios where the robot end-effector is coupled to an external body with its own dynamics. To do this we emulated a tissue manipulation task where the robot grasps and pulls on a piece of tissue which is suddenly cut and released from the surrounding tissue, resulting in a release of stored elastic energy, and significant dynamic motion. We track the dynamic motion of the tip position for comparison between model and experiment.

A. Experimental Design

The setup consists of a two-tube robot design with the outer tube passing through an acrylic base plate. Both tubes were

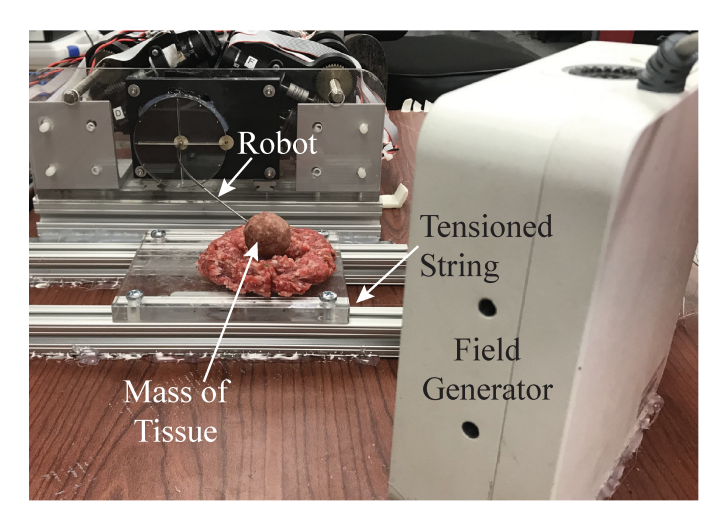


Fig. 10. The experimental setup for the tissue manipulation consists of a two-tube concentric tube robot grasping a mass of bovine tissue. A tensioned string simulating attachment to surrounding tissue is suddenly cut, releasing stored elastic energy and generating a dynamic response. A magnetic tracker measures the dynamic tip trajectory.

TABLE III
MODEL PARAMETERS FOR TISSUE EXPERIMENT

NAME	DESCRIPTION	METHOD	VALUE
$r_{i,1}$	Inner radius	Datasheet	0.514 mm
$r_{o,1}$	Outer radius	Datasheet	0.622 mm
$\boldsymbol{E_1}$	Young's modulus	Deflection test	52 GPa
$\boldsymbol{\beta}_1$	Location of actuator	Chosen	-252.1 mm
L_{1S}	Initial straight length	Fit from image	301 mm
L_{1C}	Length of curved section	Fit from image	97.1 mm
$u_{1,x}^*$	Precurvature	Fit from image	9.174 m ⁻¹
$r_{i,2}$	Inner radius	Datasheet	0.800 mm
$r_{o,2}$	Outer radius	Datasheet	1.03 mm
$\boldsymbol{E_2}$	Young's modulus	Deflection test	75 GPa
$\boldsymbol{\beta}_2$	Location of actuator	Chosen	-197.7 mm
L_{2S}	Initial straight length	Fit from image	200.0 mm
L_{2C}	Length of curved section	Fit from image	84.5 mm
$u_{2,x}^*$	Precurvature	Fit from image	$10.075 \ \mathrm{m^{-1}}$
$\rho_1 = \rho_2$	Density	Datasheet	6493 kg/m ³
\boldsymbol{B}_*	All mat. damping coeffs	Chosen	0 Nm ² s
ν	Vicious friction coeff	Calibrated prior	$1.16 \times 10^{-7} \frac{(N-m)s}{rad}$
μ'	Coulomb friction coeff	Calibrated prior	0.00323
μ'_{base}	Baseplate Coulomb coeff	Calibrated	1.09
ν′ _{base}	Baseplate Viscous coeff	Calibrated	$73.9 \times 10^{-7} \frac{(N-m)s}{rad}$
ε	Sigmoid Parameter	Chosen	15 rad/s

made of Nitinol. The measured and calibrated parameters for the robot are listed in Table III.

The grasped tissue was a spherical mass of bovine muscle having a mass of 8.0 g and a radius of 24.7 mm. The tip of the robot coincided with the center of the sphere. To simulate the grasped tissue's attachment to surrounding tissue, a fishing line was tied behind the mass, at 33.6 mm from the tip of the robot, and a weight of 60.0 g was first hung from the line and then suddenly cut, releasing stored elastic energy and generating a dynamic response. The tip motion of the robot, after cutting the fishing line, was measured with 40 Hz resolution by an Aurora magnetic tracking system (Northern Digital Inc., Waterloo, ON, CAN), where the 5 mm long

tracking marker was flush with the robot tip so that the marker was centered 2.5 mm from the tip. The tubes were actuated at angles of $\alpha_1(\beta_1) = \alpha_2(\beta_2) = \pi/2$ so that, absent the effects of weight, the robot would lie in a plane orthogonal to the direction of gravity. The combined weight of the grasped tissue and the hung weight induced significant bending in the robot. This experimental set up can be seen in Figure 10.

For a secondary validation, a similar experiment was preformed with the same robot in the same configuration; however, to test whether the calibrated parameters accurately predict the response under a different set of conditions, and to test whether or not tissue properties themselves play a significant role, a rigid sphere made of Grey Pro resin (Form-Labs, Somerville, MA, USA) of a different size and mass was attached to the tip. The sphere had a mass of 16.3 g and a radius of 15.0 mm. The fishing line was attached 15.0 mm from the tip of the robot and was tensioned with a hung mass of 30.0 g.

B. Simulation

These tissue manipulation experiments are a complementary dataset to our previous high-speed snapping experiments because the dynamic behavior involved is several orders of magnitude slower, due to the coupling to an external dynamic system. These slower dynamics also provide an opportunity to demonstrate a key benefit of our numerical method, namely the ability to take arbitrarily large time steps stably due to the implicit time discretization strategy, as discussed in [36]. Thus, an appropriate time step in this case is 3 ms, which provides ample temporal resolution and results in faster computation times relative to the speed of the physical processes involved. In fact, as we detail in the next section, in this case we can computationally simulate the dynamics faster than the actual physical system evolves (our definition of "real-time"). This larger time step also creates an ODE system in the spatial dimension which is less numerically sensitive, allowing us to solve it with a more efficient shooting method (as in [35], [36]) instead of the spatial finite difference system described in (25).

C. Parameters and Calibration

For this simulation, the BDF- α method with $\alpha=0.45$ and $\Delta t=3$ ms were used for time discretization, and 400 spatial nodes were distributed along the robot length (integrated with fourth-order Runge Kutta).

The robot parameters are listed in Table III along with how each was determined. We set the inter-tube friction coefficients (Coulomb and viscous) equal to the values that were calibrated from the snapping experiments in the previous section; however, there is an additional source of energy dissipation due to friction between the outer tube and the hole in the acrylic base plate through which it passes (this interface was not present in the snapping experiment). This interface is modeled by Equation (24), and separate frictional parameters need to be determined. A least-squares fit of the height of the first 5 peaks and troughs of the displacement magnitude

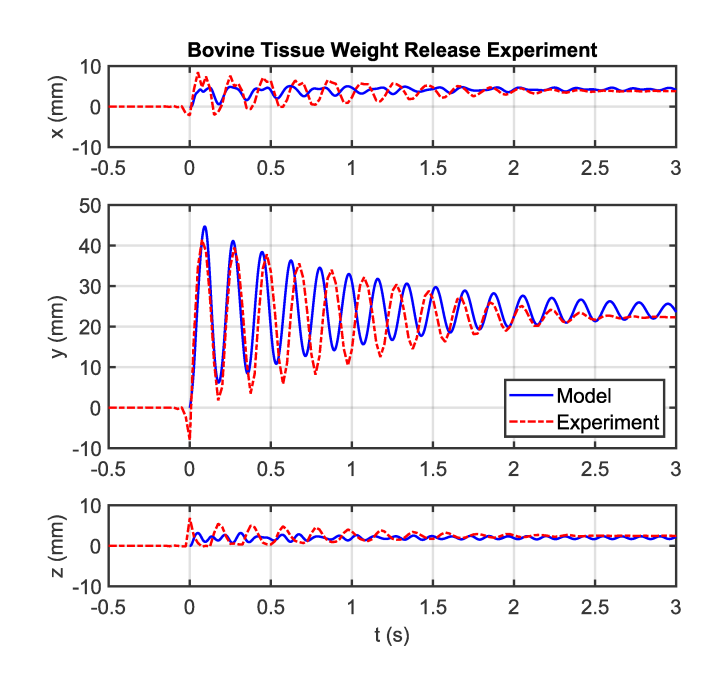


Fig. 11. To simulate resecting a tissue mass, bovine muscle was attached to the tip of the robot and a secondary mass was attached with a fishing line to simulate tissue forces. The displacement of the robot tip was measured relative to the initial static position when the secondary mass is attached. At t=0, the fishing line is cut, releasing the grasped tissue from its surroundings and causing the the robot tip to oscillate. The robot axes are aligned such that the z axis is orthogonal to the base plate and the y axis is in the direction opposite of gravity.

was performed to calibrate the effective Coulomb and viscous friction parameters at the baseplate, shown in Table III. Note that we do not necessarily expect these values to be similar to those that model the inter-tube friction because they describe a different material interface with a different clearance. The sigmoid parameter ϵ , in the friction model, was chosen to be 15 rad/s which is appropriate given the typical angular speeds exhibited in this experiment.

D. Results

The results of the calibrated model are shown in Figure 11. The data presented is the measured tip displacement from its initial static position in 3D space (the z axis is along the robot axis at the base and gravity acts in the negative y direction). The datum t=0 is aligned with the time the fishing line is cut. We can see that the decay rate of the peaks was matched well by the calibrated base friction parameters. As with the snapping tests, the initial few peaks match very well. The main manifestation of error is a slight difference in the frequency (which is mainly influenced by inertial and stiffness parameters) that results in a phase shift over time. We can also see the effects of a small amount of geometric registration error of the tracker coordinate system, which causes the z and x displacement amplitudes to appear relatively larger (rigidly rotating the dataset by a few degrees eliminates much of this error).

The calibrated friction coefficients were further tested by applying them to the secondary data set obtained from the

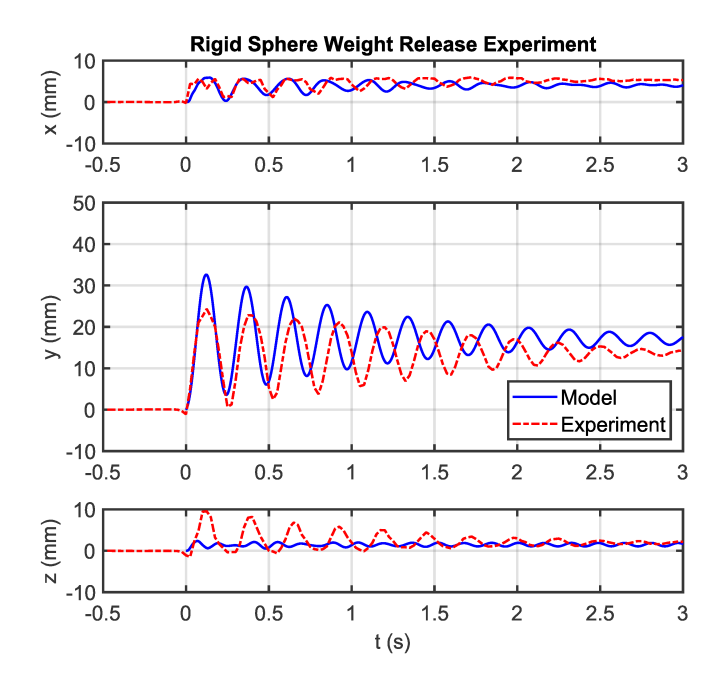


Fig. 12. To validate the calibrated friction parameters, a second experiment was done using a rigid sphere attached to the tip and a different mass attached to the fishing line. The displacement of the robot tip was measured relative to the initial static position when the secondary mass is attached. At t=0, the fishing line is cut, causing the the robot tip to oscillate. The axes are aligned such that the z axis is orthogonal to the base plate and the y axis is in the direction opposite of gravity.

rigid sphere experiments. This is shown in Figure 12, which shows similarly accurate results in terms of decay rate and frequency. We believe the steady-state error can be attributed to small errors in base-frame registration, the elastic constants in the model parameters, and imperfect model assumptions such as zero tube clearance. Note that the accuracy of the tissue manipulation experiment depends more heavily on these model parameters than the data in the snap-through experiment does, since it measures position of the tip instead of the relative angle between the tubes. The average of root-mean-squared position errors over the two tissue manipulation experiments was 9.5% of the robot length, from the base plate to the end effector, which is comparable to previous reports of accuracy in static models [15], [13].

E. Numerical Analysis

We also demonstrate that the numerical methods used for these experiments can run in real-time. That is, the model calculations necessary to simulate one second of robot motion can be completed in less than one second, so that the simulation keeps up with the physics. To quantify this, we report the real-time performance ratio (time-span simulated over required computation time) in Figure 13 for the motions executed in the tissue grasping experiment. Since large time steps can be taken, the method is highly efficient; every solution represented on the plot is real-time. Decreasing the number of spatial points used also decreases the computation time by the expected linear amount (i.e. doubling the number

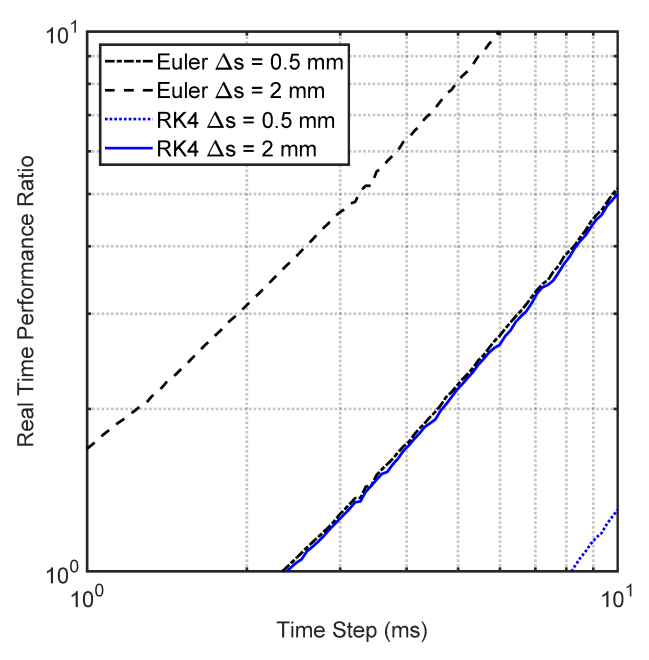


Fig. 13. This plot demonstrates the real-time performance of our model solution in the tissue experiment. The real-time performance ratio is the time span simulated divided by the wall-clock time spent running the simulation. All simulations represented in the figure were executed in real time. This ratio is affected by both time step size and spatial step size.

of points doubles the computation time).

The spatial node spacing also affects solution accuracy. Figure 14 shows the RMS difference in tip displacement over 3 seconds of motion between a benchmark numerical solution with high resolution (RK4 with time step of 3 ms and a spatial step of 0.02 mm) and solutions using a coarser step size. As expected, using RK4 in the spatial dimension significantly increases the accuracy over 1st order Euler method, at the cost of more computation time, but the trade-off is worthwhile, i.e. at time steps that require equivalent computational times, RK4 is over an order of magnitude more accurate.

VI. CONCLUSIONS

We have presented the first dynamic model for concentric tube robots by adapting the dynamic Cosserat rod PDEs to a collection of concentric precurved tubes. The model is able to capture dynamic transition behavior during the complex phenomenon of an elastic instability and the associated release of stored elastic energy. In particular, the swing-through velocity profile and overshoot behavior are captured well. It is also capable of capturing slower bending oscillations during tissue grasping in real time. This model paves the way for better understanding of dynamic effects in the future as well as the incorporation of more detailed frictional models. All of these advancements may improve the design of concentric tube robots in demanding applications. One lesson learned from our experimental analysis is that the snap-through transient dynamics are somewhat affected by mass attached to the tip of the robot. Changes in tip mass on the order of 0.02 grams were

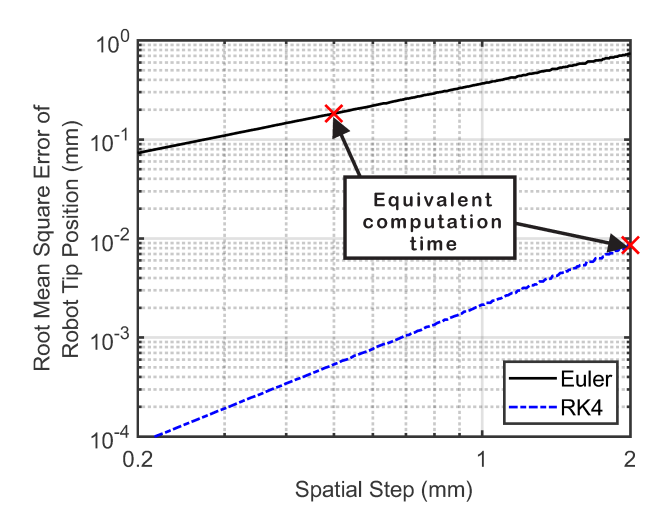


Fig. 14. RMS error with respect to a high-resolution benchmark solution is plotted as a function of spatial step size Δs , where all simulations were performed with the same time step $\Delta t=3~ms$. This plot illustrates that performing spatial integration with a high order method such as RK4 offers a much better time/accuracy trade-off. The two annotated points have equivalent computation times.

enough to change the frequency of oscillation a noticeable amount.

The decaying oscillations after the snap-through transition are not perfectly described by the model, and future work could attempt to improve model accuracy by incorporating additional effects such as clearance between tubes, a distributed friction model, or actuator/drivetrain dynamics. One limitation of our model that may be addressed in future work is that the linear velocities and accelerations of the actuator insertions, at the base of the tubes, were assumed to be negligible. This seems to be a reasonable assumption for most teleoperation scenarios, especially if the snap-through dynamics are of primary interest, but it may be less accurate under very aggressive motion plans or with slower dynamics when manipulating tissue. Introducing these terms would be nontrivial, but could lead to a more accurate model in specific situations. Future work could also expand the validation of this model on CTR's with more than two tubes.

REFERENCES

- [1] H. B. Gilbert, D. C. Rucker, and R. J. Webster III, "Concentric Tube Robots: The State of the Art and Future Directions," in *Robotics Research*, M. Inaba, , and P. Corke, Eds. Springer International Publishing, 2016, pp. 253–269.
- [2] T. K. Morimoto and A. M. Okamura, "Design of 3-D Printed Concentric Tube Robots," *IEEE Transactions on Robotics*, vol. 32, no. 6, pp. 1419– 1430, dec 2016.
- [3] J. Burgner-Kahrs, D. C. Rucker, and H. Choset, "Continuum Robots for Medical Applications: A Survey," *IEEE Transactions on Robotics*, vol. 31, no. 6, pp. 1261–1280, 2015.
- [4] A. W. Mahoney, H. B. Gilbert, and R. J. Webster, "A Review of Concentric Tube Robots: Modeling, Control, Design, Planning, and Sensing," in *The Encyclopedia of Medical Robotics*. World Scientific, oct 2016, pp. 181–202.
- [5] P. Sears and P. Dupont, "A Steerable Needle Technology Using Curved Concentric Tubes," in 2006 IEEE/RSJ International Conference on Intelligent Robots and Systems. IEEE, oct 2006, pp. 2850–2856.

- [6] M. Torabi, R. Gupta, and C. J. Walsh, "Compact Robotically Steerable Image-Guided Instrument for Multi-Adjacent-Point (MAP) Targeting," *IEEE Transactions on Robotics*, vol. 30, no. 4, pp. 802–815, aug 2014.
- [7] W. Wei, R. E. Goldman, H. F. Fine, C. Stanley, and N. Simaan, "Performance Evaluation for Multi-arm Manipulation of Hollow Suspended Organs," *IEEE Transactions on Robotics*, vol. 25, no. 1, pp. 147–157, feb 2009.
- [8] R. J. Hendrick, C. R. Mitchell, S. D. Herrell, R. J. Webster, and III, "Hand-held Transendoscopic Robotic Manipulators: A Transurethral Laser Prostate Surgery Case Study," *The International Journal of Robotics Research*, vol. 34, no. 13, pp. 1559–1572, nov 2015.
- [9] A. H. Gosline, N. V. Vasilyev, E. J. Butler, C. Folk, A. Cohen, R. Chen, N. Lang, P. J. Del Nido, and P. E. Dupont, "Percutaneous Intracardiac Beating-heart Surgery using Metal MEMS Tissue Approximation Tools," *The International Journal of Robotics Research*, vol. 31, no. 9, pp. 1081– 1093, aug 2012.
- [10] J. Burgner, D. C. Rucker, H. B. Gilbert, P. J. Swaney, P. T. Russell, K. D. Weaver, and R. J. Webster, "A Telerobotic System for Transnasal Surgery," *IEEE/ASME Transactions on Mechatronics*, vol. 19, no. 3, pp. 996–1006, jun 2014.
- [11] H. Yu, L. Wu, K. Wu, and H. Ren, "Development of a Multi-Channel Concentric Tube Robotic System With Active Vision for Transnasal Nasopharyngeal Carcinoma Procedures," *IEEE Robotics and Automation Letters*, vol. 1, no. 2, pp. 1172–1178, jul 2016.
- [12] C. Baek, K. Yoon, and D.-N. Kim, "Finite Element Modeling of Concentric-tube Continuum Robots," Structural Engineering and Mechanics, vol. 57, no. 5, pp. 809–821, mar 2016.
- [13] P. Dupont, J. Lock, B. Itkowitz, and E. Butler, "Design and Control of Concentric-Tube Robots," *IEEE Transactions on Robotics*, vol. 26, no. 2, pp. 209–225, apr 2010.
- [14] D. C. Rucker, R. J. Webster, G. S. Chirikjian, N. J. Cowan, and N. J. Cowan, "Equilibrium Conformations of Concentric-tube Continuum Robots." *The International Journal of Robotics Research*, vol. 29, no. 10, pp. 1263–1280, sep 2010.
- [15] D. C. Rucker, B. A. Jones, and R. J. Webster III, "A Geometrically Exact Model for Externally Loaded Concentric-Tube Continuum Robots," *IEEE Transactions on Robotics*, vol. 26, no. 5, pp. 769–780, oct 2010.
- [16] J. Lock, G. Laing, M. Mahvash, and P. E. Dupont, "Quasistatic Modeling of Concentric Tube Robots with External Loads," in 2010 IEEE/RSJ International Conference on Intelligent Robots and Systems, vol. 2010. IEEE, oct 2010, pp. 2325–2332.
- [17] K. Leibrandt, C. Bergeles, and G.-Z. Yang, "On-line Collision-free Inverse Kinematics with Frictional Active Constraints for Effective Control of Unstable Concentric Tube Robots," in 2015 IEEE/RSJ International Conference on Intelligent Robots and Systems (IROS). IEEE, sep 2015, pp. 3797–3804.
- [18] H. Azimian, P. Francis, T. Looi, and J. Drake, "Structurally-Redesigned Concentric-Tube Manipulators with Improved Stability," in 2014 IEEE/RSJ International Conference on Intelligent Robots and Systems. IEEE, sep 2014, pp. 2030–2035.
- [19] M. N. Boushaki, C. Liu, and P. Poignet, "Task-space Position Control of Concentric-Tube Robot with Inaccurate Kinematics using Approximate Jacobian," in 2014 IEEE International Conference on Robotics and Automation (ICRA). IEEE, may 2014, pp. 5877–5882.
- [20] R. Xu, A. Yurkewich, and R. V. Patel, "Curvature, Torsion, and Force Sensing in Continuum Robots Using Helically Wrapped FBG Sensors," *IEEE Robotics and Automation Letters*, vol. 1, no. 2, pp. 1052–1059, jul 2016.
- [21] R. Xu, A. Asadian, A. S. Naidu, and R. V. Patel, "Position Control of Concentric-Tube Continuum Robots Using a Modified Jacobian-Based Approach," in 2013 IEEE International Conference on Robotics and Automation. IEEE, may 2013, pp. 5813–5818.
- [22] J. Lock and P. E. Dupont, "Friction Modeling in Concentric Tube Robots," in 2011 IEEE International Conference on Robotics and Automation. IEEE, may 2011, pp. 1139–1146.
- [23] J. Ha, G. Fagogenis, and P. E. Dupont, "Modeling Tube Clearance and Bounding the Effect of Friction in Concentric Tube Robot Kinematics," *IEEE Transactions on Robotics*, pp. 1–18, 2018.
- [24] H. B. Gilbert, R. J. Hendrick, and R. J. Webster III, "Elastic Stability of Concentric Tube Robots: A Stability Measure and Design Test," *IEEE Transactions on Robotics*, vol. 32, no. 1, pp. 20–35, feb 2016.
- [25] J. Ha, F. C. Park, and P. E. Dupont, "Elastic stability of concentric tube robots subject to external loads," *IEEE Transactions on Biomedical Engineering*, vol. 63, no. 6, pp. 1116–1128, June 2016.

- [26] K. E. Riojas, R. J. Hendrick, and R. J. Webster, "Can Elastic Instability Be Beneficial in Concentric Tube Robots?" *IEEE Robotics and Automation Letters*, vol. 3, no. 3, pp. 1624–1630, jul 2018.
- [27] J. Ha and P. E. Dupont, "Designing Stable Concentric Tube Robots Using Piecewise Straight Tubes," *IEEE Robotics and Automation Letters*, vol. 2, no. 1, pp. 298–304, jan 2017.
- [28] J. Ha, F. C. Park, and P. E. Dupont, "Achieving Elastic Stability of Concentric Tube Robots through Optimization of Tube Precurvature," in 2014 IEEE/RSJ International Conference on Intelligent Robots and Systems. IEEE, sep 2014, pp. 864–870.
- [29] R. J. Hendrick, H. B. Gilbert, and R. J. Webster, "Designing Snap-free Concentric Tube Robots: A Local Bifurcation Approach," in 2015 IEEE International Conference on Robotics and Automation (ICRA). IEEE, may 2015, pp. 2256–2263.
- [30] J.-S. Kim, D.-Y. Lee, K. Kim, S. Kang, and K.-J. Cho, "Toward a Solution to the Snapping Problem in a Concentric-tube Continuum Robot: Grooved Tubes with Anisotropy," in 2014 IEEE International Conference on Robotics and Automation (ICRA). IEEE, may 2014, pp. 5871–5876.
- [31] C. Bergeles, A. H. Gosline, N. V. Vasilyev, P. J. Codd, P. J. del Nido, and P. E. Dupont, "Concentric Tube Robot Design and Optimization Based on Task and Anatomical Constraints," *IEEE Transactions on Robotics*, vol. 31, no. 1, pp. 67–84, feb 2015.
- [32] K. Leibrandt, C. Bergeles, and G.-Z. Yang, "Implicit Active Constraints for Safe and Effective Guidance of Unstable Concentric Tube Robots," in 2016 IEEE/RSJ International Conference on Intelligent Robots and Systems (IROS). IEEE, oct 2016, pp. 1157–1163.
- [33] —, "Concentric Tube Robots: Rapid, Stable Path-Planning and Guidance for Surgical Use," *IEEE Robotics & Automation Magazine*, vol. 24, no. 2, pp. 42–53, jun 2017.
- [34] D. C. Rucker and R. J. Webster III, "Statics and Dynamics of Continuum Robots With General Tendon Routing and External Loading," *IEEE Transactions on Robotics*, vol. 27, no. 6, pp. 1033–1044, 2011.
- [35] J. Till and D. C. Rucker, "Elastic Rod Dynamics: Validation of a Real-Time Implicit Approach," in 2017 IEEE/RSJ International Conference on Intelligent Robots and Systems (IROS). Vancouver, Canada: IEEE, sep 2017, pp. 3013–3019.
- [36] J. Till, V. Aloi, and C. Rucker, "Real-time dynamics of soft and continuum robots based on cosserat rod models," *The International Journal of Robotics Research*, vol. 38, no. 6, pp. 723–746, 2019.
- [37] S. S. Antman, Nonlinear Problems of Elasticity Second Edition. New York, NY: Springer, 2005, vol. 107.
- [38] Y. Xiong and F. Quek, "Hand motion gesture frequency properties and multimodal discourse analysis," *International Journal of Computer Vision*, vol. 69, no. 3, pp. 353–371, Sep 2006.
- [39] R. M. Murray, Z. Li, and S. Sastry, A Mathematical Introduction to Robotic Manipulation. CRC Press, 1994.
- [40] J. Linn, H. Lang, and A. Tuganov, "Geometrically Exact Cosserat Rods with Kelvin-Voigt Type Viscous Damping," *Mechanical Sciences*, vol. 4, no. 1, pp. 79–96, 2012.
- [41] R. Courant, K. Friedrichs, and H. Lewy, "On the Partial Difference Equations of Mathematical Physics," *IBM Journal of Research and Development*, vol. 11, no. 2, pp. 215–234, mar 1967.
- [42] J. Butcher, Numerical Methods for Ordinary Differential Equations. John Wiley & Sons, Inc., 2016.
- [43] C. Gatti-Bono and N. Perkins, "Physical and Numerical Modelling of the Dynamic Behavior of a Fly Line," *Journal of Sound and Vibration*, vol. 255, no. 3, pp. 555–577, 2002.
- [44] C.-C. Lan and K.-M. Lee, "Generalized Shooting Method for Analysing Compliant Mechanisms with Curved Members," *Journal of Mechanical Design*, vol. 128, no. July 2006, pp. 765–775, 2006.
- [45] C. C. Lan, K. M. Lee, and J. H. Liou, "Dynamics of Highly Elastic Mechanisms Using the Generalized Multiple Shooting Method: Simulations and Experiments," *Mechanism and Machine Theory*, vol. 44, no. 12, pp. 2164–2178, 2009.
- [46] E. A. Celaya and J. Jos, "BDF-α: A Multistep Method with Numerical Damping Control," *Universal Journal of Computational Mathematics*, vol. 1, no. 3, pp. 96–108, 2013.
- [47] C. Rucker, "Integrating Rotations using Non-Unit Quaternions," *IEEE Robotics and Automation Letters*, vol. 3, no. 4, pp. 2979–2986, 2018.
- [48] C. F. Curtiss and J. O. Hirschfelder, "Integration of Stiff Equations," Proceedings of the National Academy of Sciences of the United States of America, vol. 38, no. 3, pp. 235–43, mar 1952.

- [49] G. Guennebaud, B. Jacob, and Others, "Eigen v3," http://eigen.tuxfamily.org, 2010.
- [50] J. Zhang, R. J. Perez, and E. J. Lavernia, "Documentation of damping capacity of metallic, ceramic and metal-matrix composite materials," *Journal of Materials Science*, vol. 28, no. 9, pp. 2395–2404, 1993.



John Till (S14) is an avid programmer with degrees in mechanical engineering. He received the B.S. degree in mechanical engineering from Tennessee Technological University in 2014 and the M.S. and Ph.D. degrees in mechanical engineering in 2018 and 2019 from The University of Tennessee, where he worked in the REACH Lab. His research interests include numerical simulation, robotics, and programming languages. He is grateful to Caleb and the medical robotics community for a fun and

supportive environment to develop research skills.



Vincent Aloi (F'16) received the B.S. degree in mechanical engineering from the University of Tennessee, Knoxville, TN in 2016. He is currently pursuing a Ph.D. degree in mechanical engineering from the University of Tennessee, Knoxville, TN, as a graduate research assistant in the REACH lab. His research interests include modeling, force sensing, and continuum robotics.



Katherine Riojas (S'16) received the B.S. degree in mechanical engineering from The University of Tulsa, OK, in 2016. She is currently pursuing the Ph.D. degree at Vanderbilt University, Nashville, TN, in mechanical engineering. She is an NSF Graduate Research Fellow and received the NCAA Walter Byers award in 2016. At Vanderbilt, she works in the Medical Engineering and Discovery Lab and in the Computer-Assisted Otologic Surgery Lab. She is passionate about developing innovative

medical device solutions to existing challenges.



Patrick L. Anderson received the B.S. degree in mechanical engineering from Calvin College, Grand Rapids, MI, USA, in 2015. He is currently working toward the Ph.D. degree in mechanical engineering at Vanderbilt University, Nashville, TN, USA, in the Medical Engineering and Discovery Laboratory. His research interests include medical devices, continuum robotics, and surgical robotics. He received the NSF Graduate Research Fellowship in 2017.



Robert J. Webster III (S'97–M'08–SM'14) received the B.S. degree in electrical engineering from Clemson University, Clemson, SC, USA, in 2002, and the M.S. and Ph.D. degrees in mechanical engineering from Johns Hopkins University, Baltimore, MD, USA, in 2004 and 2007, respectively. In 2008, he joined the Faculty of Vanderbilt University, Nashville, TN, USA, where he is currently a Richard A. Schroeder Professor of Mechanical Engineering, and also a professor of electrical engineering, otolaryngology, neurological surgery, urologic surgery,

and medicine (interventional pulmonology). He directs the Medical Engineering and Discovery Laboratory, and co-founded Vanderbilt Institute for Surgery and Engineering, which brings together physicians and engineers to solve challenging clinical problems. He co-founded and serves as President of Virtuoso Surgical, Inc., and EndoTheia, Inc., Nashville, TN, USA. He has received the IEEE RAS Early Career Award, the NSF CAREER Award, the RSS Early Career Spotlight Award, the IEEE Volz Award, and the Vanderbilt Engineering Award for Excellence in Teaching. He has served as Chair of the SPIE Image-Guided Procedures, Robotic Interventions, and Modeling Conference, Associate Editor of IEEE Transactions on Robotics, and currently serves as Associate Editor for the International Journal of Robotics Research and as a charter member of the NIH Imaging Guided Interventions and Surgery study section. His research interests include surgical robotics, image-guided surgery, and continuum robotics.



D. Caleb Rucker (Member, IEEE) received the B.S. degree in engineering mechanics and mathematics from Lipscomb University, Nashville, TN, USA, in 2006, and the Ph.D. degree in mechanical engineering from Vanderbilt University, Nashville, in 2011. He is currently an Associate Professor of Mechanical Engineering at The University of Tennessee, Knoxville, TN, USA, where he directs the Robotics, Engineering, and Continuum Mechanics in Healthcare Laboratory (REACH Lab). Dr. Rucker was a recipient of the NSF CAREER Award in 2017,

and he currently serves as an Associate Editor for IEEE Transactions on Robotics.